

Late Miocene onset of the modern Antarctic Circumpolar Current

Received: 17 October 2022

Accepted: 6 December 2023

Published online: 18 January 2024

 Check for updates

Dimitris Evangelinos^{1,2}✉, Johan Etourneau^{3,4}, Tina van de Flierdt², Xavier Crosta³, Catherine Jeandel⁵, José-Abel Flores⁶, David M. Harwood⁷, Luis Valero^{1,8}, Emmanuelle Ducassou³, Isabel Sauermilch⁹, Andreas Klocker¹⁰, Isabel Cacho¹, Leopoldo D. Pena¹, Katharina Kreissig², Mathieu Benoit¹¹, Moustafa Belhadj⁵, Eduardo Paredes¹, Ester Garcia-Solsona¹, Adrián López-Quirós¹², Ariadna Salabarnada¹³ & Carlota Escutia¹⁴

The Antarctic Circumpolar Current plays a pivotal role in global climate through its strong influence on the global overturning circulation, ocean heat and CO₂ uptake. However, when and how the Antarctic Circumpolar Current reached its modern-like characteristics remains disputed. Here we present neodymium isotope and sortable silt records from sediment cores in the Southwest Pacific and South Indian oceans spanning the past 31 million years. Our data indicate that a circumpolar current like that of today did not exist before the late Miocene cooling. These findings suggest that the emergence of a homogeneous and deep-reaching strong Antarctic Circumpolar Current was not linked solely to the opening and deepening of Southern Ocean Gateways triggering continental-scale Antarctic Ice Sheet expansion during the Eocene–Oligocene Transition (~34 Ma). Instead, we find that besides tectonic pre-conditioning, the expansion of the Antarctic Ice Sheet and sea ice since the middle Miocene Climate Transition (~14 Ma) played a crucial role. This led to stronger density contrast and intensified Southern Westerly Winds across the Southern Ocean, establishing a vigorous deep-reaching circumpolar flow and an enhanced global overturning circulation, which amplified the late Cenozoic global cooling.

The Antarctic Circumpolar Current (ACC), driven by the interplay among Southern Westerly Winds (SWW), buoyancy forcing and bathymetry¹, is the largest ocean current on Earth. It actively regulates the transport of heat, moisture, carbon and nutrients between the Southern

Ocean and the low-latitude regions, thus substantially influencing atmospheric CO₂ and global climate¹. To assess the future response of the ACC to ongoing climate warming and its impacts on Antarctic Ice Sheet dynamics, global circulation and climate², it is critical to unravel

¹GRC Geociències Marines, Departament de Dinàmica de la Terra i de l'Oceà, Universitat de Barcelona, Barcelona, Spain. ²Department of Earth Science and Engineering, Imperial College London, London, UK. ³Univ. Bordeaux, CNRS, Bordeaux INP, EPOC, UMR 5805, Pessac, France. ⁴EPHE, PSL Research University, Paris, France. ⁵LEGOS (UT3, CNRS, CNES, IRD) Observatoire Midi Pyrénées, Toulouse, France. ⁶Department of Geology, University of Salamanca, Salamanca, Spain. ⁷Department of Earth and Atmospheric Sciences, University of Nebraska, Lincoln, NE, USA. ⁸Paleomagnetic Laboratory CCiTUB-Geo3Bcn, Geosciences Barcelona CSIC, Barcelona, Spain. ⁹Institute for Marine and Antarctic Studies, University of Tasmania, Hobart, Tasmania, Australia. ¹⁰NORCE Norwegian Research Centre, Bjerknes Centre for Climate Research, Bergen, Norway. ¹¹GET- Observatoire Midi Pyrénées, Toulouse, France. ¹²Department of Stratigraphy and Paleontology, University of Granada, Granada, Spain. ¹³TECNOAMBIENTE, Barcelona, Spain. ¹⁴Instituto Andaluz de Ciencias de la Tierra, CSIC-Univ. de Granada, Armilla, Spain. ✉e-mail: devangelinos@ub.edu

the timing and processes that led to the development of the modern-like deep-reaching and homogeneous ACC (circumpolar flow extending from the surface to the seafloor), a topic that has been debated for more than four decades^{3–10}.

One precondition for the inception of the ACC is the deep tectonic opening of two gateways that blocked circumpolar flow in the geological past: the Tasmanian Gateway and the Drake Passage (Fig. 1). Tectonic deepening of the Tasmanian Gateway has been constrained between ~33.5 and 30.0 million years ago (Ma) (ref. 11), which matches recent reconstructions of a deep eastward flow from the South Indian Ocean to the South Pacific Ocean at ~30 Ma, as the Tasmanian Gateway aligned with the SWW⁸. However, estimates for the deep opening of Drake Passage are still debated and range from the Oligocene (~34 Ma) to the late Miocene (~12 Ma) (refs. 5,7,9,12). Furthermore, recent work has questioned whether the tectonic opening of gateways alone is sufficient to initiate a deep-reaching and vigorous ACC similar to today's¹³. Moreover, eddy-resolving ocean model simulations show that even enhanced SWW are not able to generate a modern-like ACC when both gateways are open, suggesting that buoyancy forcing plays a primary control over the ACC transport^{14,15}.

Diagnostic features of the modern ACC

In light of the ambiguous evidence for the inception of the modern-like ACC, we present new geological data to constrain two of its diagnostic features: (1) a homogeneous neodymium (Nd) isotope signature of Circumpolar Deep Waters (CDW) across the Southern Ocean (compilation from ref. 16 and references therein) and (2) a deep-reaching strong flow (flow speed > 10 cm s⁻¹) (ref. 17).

Our new records were generated from two well-dated sediment cores (Methods and Extended Data Figs. 1 and 2) recovered at Deep Sea Drilling Project (DSDP) Site 278 located in the Southern Emerald Basin (Pacific sector of the Southern Ocean; 56° 33.42' S, 160° 04.29' E, 3,675 m water depth)¹⁸ and Ocean Drilling Program (ODP) Site 744 located on the Southern Kerguelen Plateau (Indian sector of the Southern Ocean; 61° 34.66' S, 80° 35.43' E, 2,307 m water depth)¹⁹ (Fig. 1). Both sites were persistently positioned within the main pathway of the ACC since the early Oligocene (31 Ma) and cover the depth range of the modern CDW (~2,500 and 3,500 m, respectively)^{10,20}.

Fossil fish debris from Sites 744 and 278 robustly preserved a seawater Nd isotope signature^{10,20} (Supplementary Information and Extended Data Figs. 3 and 4), and results can be used to reconstruct water-mass homogeneity along the ACC flow path ($\epsilon_{Nd(t)}$ denotes the time-corrected deviation of a measured ¹⁴³Nd/¹⁴⁴Nd ratio from the chondritic uniform reservoir in parts per 10,000 (ref. 21); Methods). Mean sortable silt (\overline{SS}) size (10–63 μ m) of terrigenous sediment fractions, can be used to reconstruct bottom flow speed²² (Supplementary Information and Extended Data Fig. 5). Combined, the proxies offer a unique and robust approach to determine the initiation of the modern-like, deep-reaching and vigorous ACC.

Onset of a homogeneous circumpolar Nd isotope fingerprint

At Site 744 (Southern Kerguelen Plateau; Fig. 1), fish debris $\epsilon_{Nd(t)}$ values range from -9.9 ± 0.1 to -7.8 ± 0.2 between the early Miocene (23.5 Ma) and the early Pleistocene (1.2 Ma) (Fig. 2b). These values are in good agreement with published Nd isotope palaeorecords from the South Atlantic and Indian oceans during the same period ($\epsilon_{Nd(t)} = \sim -7$ to -10) (Fig. 3 and Extended Data Fig. 6), suggesting an efficient exchange of deep waters between the Atlantic and the Indian sectors of the Southern Ocean since the Oligocene^{20,23,24}. Modern CDW show a similar range in Nd isotope compositions ($\epsilon_{Nd} = -8.3 \pm 1.5$, $n = 158$; compilation from ref. 16 and references therein) (Fig. 2b), implying that Site 744 was bathed by a deep water mass resembling modern CDW ϵ_{Nd} values throughout the study interval.

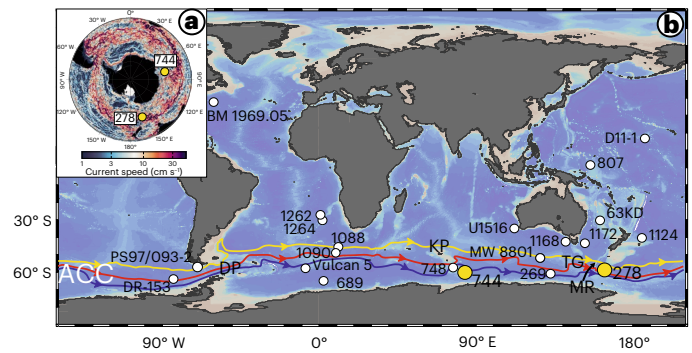


Fig. 1 | Southern Ocean circulation and core locations. **a**, Map of current speeds in the Southern Ocean and location of our study sites (yellow dots): DSDP 278 and ODP 744. Warmer red colours represent higher current speeds. **b**, ACC fronts (mean positions), Subantarctic Front (yellow), Polar Front (red) and Southern ACC Front (blue). For information of each site and references, see Extended Data Fig. 6. DP, Drake Passage; TG, Tasmanian Gateway; KP, Kerguelen Plateau; MR, Macquarie Ridge. Data in **b** for the ACC front, Subantarctic Front, Polar Front and Southern ACC Front from ref. 48. Panel **a** adapted with permission from ref. 1, Springer Nature Limited. Panel **b** created with Ocean Data View⁴⁹.

By contrast, $\epsilon_{Nd(t)}$ values at Site 278 in the Southwest Pacific are consistently more radiogenic ($\epsilon_{Nd(t)} \approx -6.0 \pm 0.2$ to -7.4 ± 0.3) than published palaeorecords from Atlantic and Indian sectors of the Southern Ocean, as well as the modern-like CDW ϵ_{Nd} values¹⁶ until the middle Miocene (~15 Ma) (Figs. 2b and 3). This indicates a fundamentally different deep ocean circulation pattern in the Pacific sector of the Southern Ocean until the middle Miocene, compared with today. Our data hence imply the absence of a modern-like efficient deep-water exchange between the Indian and the Pacific sectors of the Southern Ocean during the Oligocene and early Miocene.

Overall, variations in $\epsilon_{Nd(t)}$ values at Site 744 are controlled by the admixture of Atlantic (more unradiogenic, lower values) and Pacific (more radiogenic, higher values) waters into CDW, with potential minor influence of Antarctic weathering inputs²⁰. In detail, between the early and middle Miocene (~21–14.5 Ma), Nd isotopes at Site 744 evolve towards more unradiogenic values (Fig. 2b). This trend has previously been observed in Nd isotope palaeorecords from the Walvis Ridge (Sites 1262 and 1264)²³ and Agulhas Ridge (Site 1090)²⁴ (Extended Data Fig. 6) and been attributed to increased inflow of North Component Water (precursor of North Atlantic Deep Water) into CDW, probably via a stronger Atlantic meridional overturning circulation between the early and middle Miocene²³. The fact that absolute Nd isotope values at Kerguelen Site 744 are lower than those observed around the Agulhas Ridge Site 1090 can probably be attributed to entrainment of unradiogenic dissolved Nd from old continental sources in Prydz Bay²⁵.

Between ~14.5 and 12.0 Ma, $\epsilon_{Nd(t)}$ values at Site 744 exhibit a shift towards more radiogenic values (Fig. 2b), probably reflecting increased inflow of Pacific waters to CDW via Drake Passage. This timing coincides with geophysical, geological and geochemical evidence suggesting major tectonic changes in Drake Passage (development of a deep oceanic gateway along the southern Scotia Sea Ridge during the middle Miocene¹² and the final opening of a deep oceanic pathway in the central Scotia Sea at ~12 Ma⁷). Hence, our new data, in conjunction with tectonic reconstructions, provide strong evidence for the final establishment of a deep eastward oceanic circulation via Drake Passage at 12 Ma.

The more radiogenic $\epsilon_{Nd(t)}$ values at Site 278 in the Southwest Pacific between the Oligocene and early Miocene have previously been attributed to a stronger influence of South Pacific Deep Water ($\epsilon_{Nd(t)} \approx -6$)²⁶ in the Southern Emerald Basin because of a shallower and weaker ACC flow entering the Southwest Pacific through the Tasmanian Gateway¹⁰. Our new Nd isotope data reveal that this circulation pattern persisted

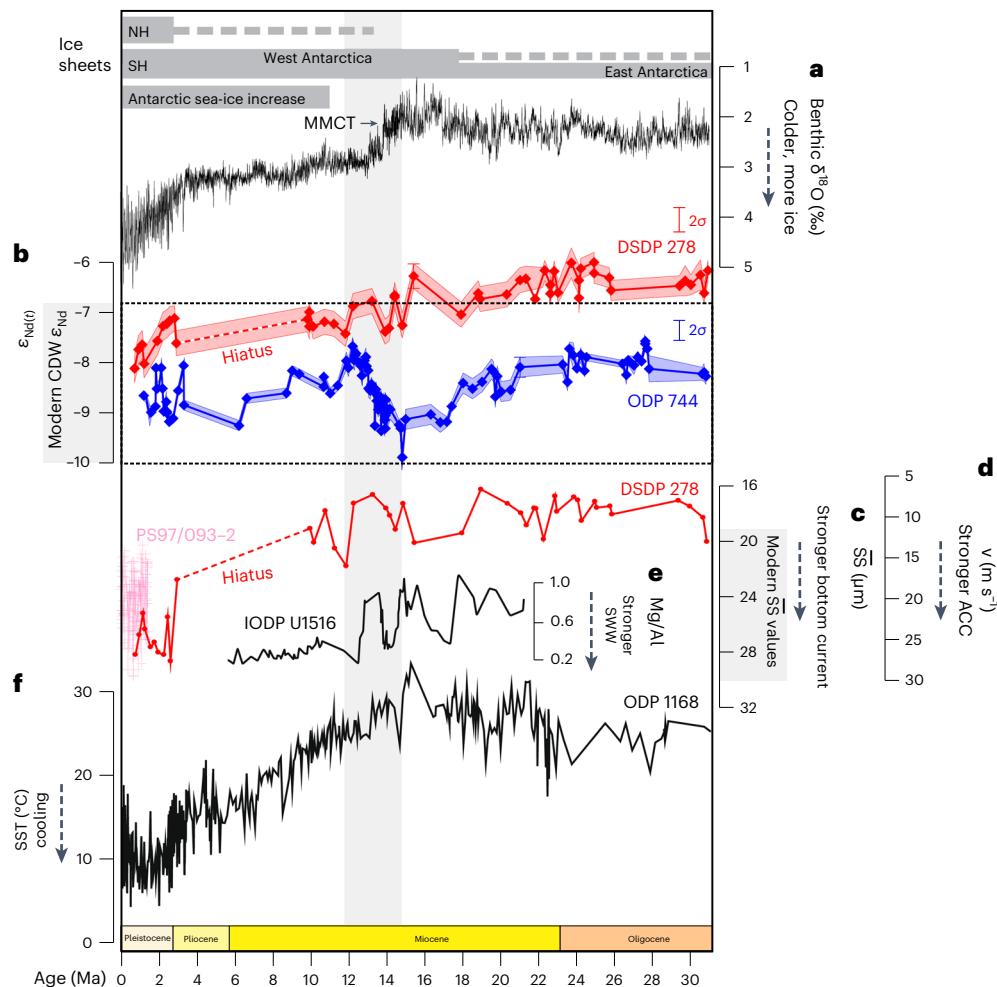


Fig. 2 | Evolution of global climate, Antarctic Circumpolar Current and Southern Ocean climate over the past 31 Myr. a, Global benthic foraminiferal $\delta^{18}\text{O}$ records⁴¹. Antarctic sea-ice increase is based on refs. 32,42. **b**, $\epsilon_{\text{Nd}(t)}$ of fish debris at DSDP Site 278. Site 278 $\epsilon_{\text{Nd}(t)}$ from 30.9 to 21.8 Ma are from ref. 10. $\epsilon_{\text{Nd}(t)}$ of fish debris at ODP Site 744. Site 744 $\epsilon_{\text{Nd}(t)}$ from 30.9 to 23.6 Ma are from ref. 20. Error envelopes and error bars represent instrumental uncertainty (2σ). Present-day CDW ϵ_{Nd} endmember along the ACC is shown in grey, compilation by ref. 16 and references therein. **c**, New mean sortable silt record from DSDP Site

278 ($\overline{\text{SS}}$) (analytical error $\pm 3\%$) and PS97/093-2 (pink stars) from ref. 29. **d**, Calculated ACC flow speeds from DSDP Site 278 (V) and PS97/093-2 (pink stars) (error estimates $\pm 12.5\%$)²². Modern-like mean $\overline{\text{SS}}$ values along the ACC are based on cores located in the DP^{29–31}. **e**, SWW evolution in Southwest Australia based on Mg/Al data ($n = 140$; analytical error less than 5%) from IODP U1516 (ref. 44). **f**, Sea surface temperature (SST) from ODP Site 1168 (refs. 39,50). MMCT, middle Miocene Climatic Transition; NH, Northern Hemisphere; SH, Southern Hemisphere.

until the middle Miocene (~ 15 Ma), supported by results from climate models showing a limited throughflow of the ACC across the Tasmanian Gateway during the Oligocene in response to a more restricted Australian palaeobathymetry²⁷ and a generally weaker global overturning circulation. The latter has been attributed to weaker SWW as a result of reduced meridional surface temperature gradients during the early to middle Miocene²⁸.

Our $\epsilon_{\text{Nd}(t)}$ values at Site 278 show an increasing influence of unradiogenic Nd in the Southwest Pacific Ocean since the early Miocene (~ 21 Ma) and the convergence with the palaeorecords from the Atlantic/Indian Ocean (Fig. 3) and modern CDW Nd isotope values from the middle Miocene (~ 15 Ma) (Fig. 2b). Given the palaeodepth ($\sim 3,500$ m) and location of Site 278 in the main pathway of the ACC¹⁰, close to the Subantarctic Front, our Nd isotope record can be explained by either (1) an increasing contribution of unradiogenic Nd from Atlantic/Indian deep waters into the deep Southwest Pacific via the Tasmanian Gateway or (2) a weakening influence of radiogenic Nd from Pacific Ocean deep waters. Published Nd isotope data from the Pacific Ocean are inconsistent with a weakening of Pacific deep-water export²⁶ (Fig. 3). We therefore propose an increasing contribution of Atlantic/Indian

deep waters, flowing through the Tasmanian Gateway and occupying the deep/abyssal Southwest Pacific, as the source of unradiogenic Nd since the early Miocene. The trend towards more unradiogenic values at Site 278 is consistent with Nd records from the Indian and Atlantic sectors of the Southern Ocean supporting further our hypothesis^{20,23,24}. The $\epsilon_{\text{Nd}(t)}$ values at Site 278 converge with Nd isotope palaeorecords from the Atlantic/Indian Ocean, as well as the modern CDW ϵ_{Nd} values¹⁶ from the middle Miocene (~ 15 Ma), but consistently only since ~ 12 Ma (Figs. 2b and 3).

Causes of modern-like deep ACC development

The convergence of our two new $\epsilon_{\text{Nd}(t)}$ records from Sites 744 and 278 around 12 Ma marks the emergence of a well-mixed CDW of the ACC and thus the development of a modern-like continuous deep-water connection among all three major oceanic basins of the Southern Ocean (Fig. 2b), which is substantially later than previously suggested^{3,4,6,8,9}. However, was the ACC also characterized by a vigorous, deep-reaching flow similar to that of today from the middle Miocene?

Our new SS data from Site 278 provide strong evidence that deep ACC speed remains relatively low until at least the late Miocene

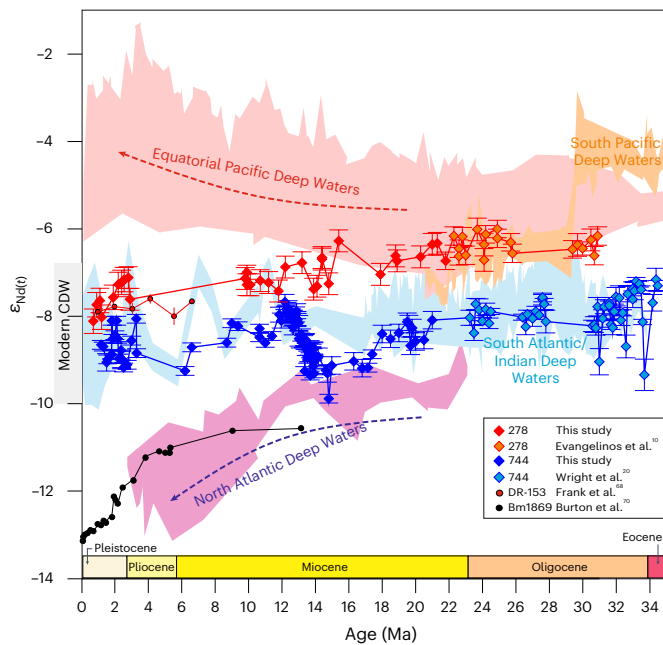


Fig. 3 | Comparison of fish debris $\epsilon_{Nd(t)}$ data from DSDP Site 278 and ODP Site 744 with other authigenic Nd records (fish debris and ferromanganese crusts) from the Atlantic, Indian and Pacific oceans. For site information, locations, designed endmembers and references, see Extended Data Fig. 6.

(~ 10 Ma) (Fig. 2c). On the basis of the calibration of \overline{SS} for the Scotia–Weddell Sea region²², our data show a mean ACC flow speed of ~ 10 cm s⁻¹ in the Southwest Pacific (Site 278) from the Oligocene to the late Miocene (~ 31 – 10 Ma; Fig. 2d). This value is two times lower than the ACC flow in Drake Passage (core PS97/093-2)²⁹, and the mean modern deep ACC velocities (~ 20 cm s⁻¹) (refs. 29–31) (Fig. 2d). Our data therefore suggest that despite the development of a continuous, deep-water circumpolar connection across the Southern Ocean since the middle Miocene (~ 12 Ma), the ACC never resembled that of the present-day vigorous deep flow speeds until at least the late Miocene (~ 10 Ma). Recent geochemical, sedimentological and micropalaeontological data across both sides of the Tasmanian Gateway support our findings, suggesting the presence of a weak ACC in the Southern Ocean compared with today’s until at least the late Miocene (~ 11 Ma)^{32–36}.

By contrast, our reconstruction of \overline{SS} -derived flow speeds shows an $\sim 50\%$ increase of the deep ACC in the Southwest Pacific (Site 278) during the Pleistocene, converging with deep ACC flow speeds in Drake Passage (PS97/093-2)²⁹ as well as modern-like vigorous deep-reaching ACC values^{29–31} (Fig. 2c,d). This major increase in deep ACC flow speed appears after a hiatus between ~ 10 and 3 Ma, which together with a prominent seismic unconformity in the Emerald Basin have been attributed to erosion associated with a local intensification of the ACC in response to the tectonic opening of the deep gap in Macquarie Ridge at 53.5° S³⁷. Today, 30% of the total transport of the ACC passes through this gap with mean speeds higher than 20 cm s⁻¹ at $3,000$ m (ref. 17). To test this hypothesis, we used the high-resolution ($1/20^\circ$ grid spacing) Massachusetts Institute of Technology general circulation model with an open (modern-day) and closed Macquarie Ridge passage (Methods). Our results show the absence of a prominent change in surface and bottom current velocities at Site 278 in response to the tectonic opening of the gap (Extended Data Fig. 7). In fact, bottom current velocities along the eastern flank of the Macquarie Ridge and across the location of Site 278 change by less than 10 cm s⁻¹ due to its opening. Our modelling results therefore argue against the possibility that a regional tectonic event in the Macquarie Ridge could have been a major driver of the observed changes in the deep ACC flow velocities in the Southwest Pacific.

Instead of tectonic changes in the Southern Ocean gateways and Macquarie Ridge region, we propose that climate-driven mechanisms drove the emergence of modern-like strong deep ACC flow. Continued sea surface^{38–40} and deep-water^{38,41} cooling in the Southern Ocean (Fig. 2f), as well as a large expansion of the Antarctic Ice Sheet^{38,41} and a more persistent presence of sea ice (Fig. 2a)^{32,42} since the middle Miocene Climatic Transition led to steepening of Equator–pole temperature gradients^{39,40} and hence a stronger density gradient^{14,15} and intensification of the SWW (Fig. 2e)^{43,44} across the Southern Ocean. This change in buoyancy forcing and wind stress in turn led to substantial intensification of the deep ACC flow. Our hypothesis is supported by our \overline{SS} data (Fig. 2c), which despite their low resolution, appear to closely track changes of the SWW as reflected in enhanced precipitation and river run-off in Southwest Australia^{43,44} (Fig. 2e), sea surface temperature cooling trend offshore Tasmania (Fig. 2f)³⁹ and eddy-resolving ocean model simulations⁴⁵. Both processes (wind stress and buoyancy forcing) modulated the strength of the ACC, with the buoyancy forcing providing the primary control over the ACC transport as shown by eddy-resolving ocean models^{14,15}. Although the presence of the late Miocene–Late Pliocene hiatus did not allow us to decipher the exact timing of inception of strong modern-like ACC deep flow velocities in the Southwest Pacific, circum-Antarctic sedimentological data provide additional evidence for the onset of a vigorous deep ocean current system in the Southern Ocean since the late Miocene as reflected by the onset and intensification of sediment drift formation^{46,47}. Regardless of the exact timing of the onset of vigorous deep ACC flow, our findings provide solid evidence that deep ACC flow did not resemble modern-like velocities before the late Miocene (~ 10 Ma) and indicate that the emergence of the modern-like vigorous deep ACC was a result of an enhanced density contrast and intensified SWW across the Southern Ocean driven by the increased Antarctic glaciation and sea-ice production.

By providing direct proxy-based evidence for the absence of a vigorous, deep-reaching ACC before ~ 10 Ma, our data challenge long-held inferences that the modern ACC development was controlled solely by the opening of Southern Ocean gateways during and after the Eocene–Oligocene Transition (~ 34 Ma). Furthermore, our findings demonstrate that the development of the ACC did not trigger the Antarctic Ice Sheet expansion during the Eocene–Oligocene Transition. Instead, the onset of the modern-like, deep-reaching ACC was a result of an enhanced density contrast and the intensification of the SWW across the Southern Ocean driven by the increased Antarctic glaciation following the middle Miocene Climatic Optimum. Our results suggest that the development of a strong deep-reaching ACC may have played an active role in global cooling by enhancing the global overturning circulation and subsequent drawdown of atmospheric CO₂ that characterized the late Cenozoic climate⁴¹.

Online content

Any methods, additional references, Nature Portfolio reporting summaries, source data, extended data, supplementary information, acknowledgements, peer review information; details of author contributions and competing interests; and statements of data and code availability are available at <https://doi.org/10.1038/s41561-023-01356-3>.

References

- Rintoul, S. R. The global influence of localized dynamics in the Southern Ocean. *Nature* **558**, 209–218 (2018).
- Meredith, M. et al. in *Special Report on the Ocean and Cryosphere in a Changing Climate* (eds Pörtner, H.-O. et al.) 203–320 (Cambridge Univ. Press, 2019).
- Kennett, J. P. Cenozoic evolution of Antarctic glaciation, the circum-Antarctic Ocean, and their impact on global paleoceanography. *J. Geophys. Res.* **82**, 3843–3860 (1977).

4. Pfuhl, H. A. & McCave, I. N. Evidence for late Oligocene establishment of the Antarctic Circumpolar Current. *Earth Planet. Sc. Lett.* **235**, 715–728 (2005).
5. Barker, P. F., Filippelli, G. M., Florindo, F., Martin, E. E. & Scher, H. D. Onset and role of the Antarctic Circumpolar Current. *Deep Sea Res. II* **54**, 2388–2398 (2007).
6. Lyle, M., Gibbs, S., Moore, T. C. & Rea, D. K. Late Oligocene initiation of the Antarctic Circumpolar Current: evidence from the South Pacific. *Geology* **35**, 691–694 (2007).
7. Dalziel, I. W. D. et al. A barrier to deep Antarctic circumpolar flow until the late Miocene? *Geology* **41**, 947–950 (2013).
8. Scher, H. D. et al. Onset of Antarctic circumpolar current 30 million years ago as Tasmanian Gateway aligned with westerlies. *Nature* **523**, 580–583 (2015).
9. Hodel, F. et al. Drake Passage gateway opening and Antarctic Circumpolar Current onset 31 Ma ago: the message of foraminifera and reconsideration of the neodymium isotope record. *Chem. Geol.* **570**, 120171 (2021).
10. Evangelinos, D. et al. Absence of a strong, deep-reaching Antarctic Circumpolar Current zonal flow across the Tasmanian Gateway during the Oligocene to early Miocene. *Glob. Planet. Change* **208**, 103718 (2022).
11. Stickley, C. E. et al. Timing and nature of the deepening of the Tasmanian Gateway. *Paleoceanography* **19**, PA4027 (2004).
12. Pérez, L. F. et al. Oceanographic and climatic consequences of the tectonic evolution of the southern Scotia Sea Basins, Antarctica. *Earth Sci. Rev.* **198**, 102922 (2019).
13. Sauermilch, I. et al. Gateway-driven weakening of ocean gyres leads to Southern Ocean cooling. *Nat. Commun.* **12**, 6465 (2021).
14. Hogg, A. McC. An Antarctic Circumpolar Current driven by surface buoyancy forcing. *Geophys. Res. Lett.* **37**, L23601 (2010).
15. Munday et al. Eddy saturation of equilibrated circumpolar currents. *Arch. Med. Sci.* **43**, 507–532 (2013).
16. Lambelet, M. et al. The neodymium isotope fingerprint of Adèle Coast Bottom Water. *Geophys. Res. Lett.* **45**, 11247–11256 (2018).
17. Rintoul, S. R. et al. Antarctic Circumpolar Current transport and barotropic transition at Macquarie Ridge. *Geophys. Res. Lett.* **41**, 7254–7261 (2014).
18. Shipboard Scientific Party. Site 278. In *Proc. Deep Sea Drilling Project Initial Reports* Vol. 29 (eds Kennett, J. P. et al.) 121–190 (DSDP, 1975).
19. Shipboard Scientific Party. Site 744. In *Proc. Ocean Drilling Program Initial Reports* 1.Vol. 119 (eds Barron, J. et al.) 477–504 (ODP, 1989).
20. Wright, N. M. et al. No change in Southern Ocean circulation in the Indian Ocean from the Eocene through late Oligocene. *Paleoceanogr. Paleoclimatol.* **33**, 152–167 (2018).
21. Jacobsen, S. B. & Wasserburg, G. J. Sm–Nd isotopic evolution of chondrites. *Earth Planet. Sci. Lett.* **50**, 139–155 (1980).
22. McCave, I. N., Thornalley, D. J. R. & Hall, I. R. Relation of sortable silt grain-size to deep-sea current speeds: calibration of the ‘Mud Current Meter’. *Deep-Sea Res. I* **127**, 1–12 (2017).
23. Via, R. & Thomas, D. J. Evolution of Atlantic thermohaline circulation: early Oligocene onset of deep-water production in the North Atlantic. *Geology* **35**, 441–444 (2006).
24. Scher, H. D. & Martin, E. E. Oligocene deep water export from the North Atlantic and the development of the Antarctic Circumpolar Current examined with neodymium isotopes. *Paleoceanography* **23**, PA1205 (2008).
25. van de Flierdt et al. Evidence against a young volcanic origin of the Gamburtsev Subglacial Mountains, Antarctica. *Geophys. Res. Lett.* **35**, LS21303 (2008).
26. McKinley, C. C., Thomas, D. J., LeVay, L. & Rolewicz, Z. Nd isotopic structure of the Pacific Ocean 40–10 Ma, and evidence for the reorganization of deep North Pacific Ocean circulation between 36 and 25 Ma. *Earth Planet. Sc. Lett.* **521**, 139–149 (2019).
27. Hill, D. J. et al. Paleogeographic controls on the onset of the Antarctic Circumpolar Current. *Geophys. Res. Lett.* **40**, 5199–5204 (2013).
28. Herold, N. et al. Modeling the Miocene Climatic Optimum: ocean circulation. *Paleoceanography* **27**, PA1209 (2012).
29. Toyos, M. H. et al. Antarctic Circumpolar Current dynamics at the Pacific entrance to the Drake Passage over the past 1.3 million years. *Paleoceanogr. Paleoclimatol.* **35**, e2019PA003773 (2020).
30. Wu, S. et al. Orbital- and millennial-scale Antarctic Circumpolar Current variability in Drake Passage over the past 140,000 years. *Nat. Commun.* **12**, 3948 (2021).
31. McCave, I. N., Crowhurst, S. J., Kuhn, G., Hillenbrand, C.-D. & Meredith, M. P. Minimal change in Antarctic Circumpolar Current flow speed between the last glacial and Holocene. *Nat. Geosci.* **7**, 113–116 (2014).
32. Sangiorgi, F. et al. Southern Ocean warming and Wilkes Land ice sheet retreat during the mid-Miocene. *Nat. Commun.* **9**, 317 (2018).
33. Bijl, P. K. et al. Paleoceanography and ice sheet variability offshore Wilkes Land, Antarctica – Part 2: Insights from Oligocene–Miocene dinoflagellate cyst assemblages. *Clim. Past* **14**, 1015–1033 (2018).
34. Hartman, J. D. et al. Paleoceanography and ice sheet variability offshore Wilkes Land, Antarctica – Part 3: insights from Oligocene–Miocene TEX₈₆-based sea surface temperature reconstructions. *Clim. Past* **14**, 1275–1297 (2018).
35. Salabarnada, A. et al. Paleoceanography and ice sheet variability offshore Wilkes Land, Antarctica – Part 1: insights from late Oligocene astronomically paced contourite sedimentation. *Clim. Past* **14**, 991–1014 (2018).
36. Evangelinos, D. et al. Late Oligocene–Miocene proto-Antarctic Circumpolar Current dynamics off the Wilkes Land margin, East Antarctica. *Glob. Planet. Change* **191**, 103221 (2020).
37. Schuur, C. L. et al. Sedimentary regimes at the Macquarie Ridge Complex: interaction of Southern Ocean circulation and plate boundary bathymetry. *Paleoceanography* **13**, 646–670 (1998).
38. Leutert, T. J. et al. Coupled Southern Ocean cooling and Antarctic ice sheet expansion during the middle Miocene. *Nat. Geosci.* **13**, 634–639 (2020).
39. Hou, S. et al. Lipid-biomarker-based sea surface temperature record offshore Tasmania over the last 23 million years. *Clim. Past* **19**, 787–802 (2023).
40. Herbert, T. D. et al. Late Miocene global cooling and the rise of modern ecosystems. *Nat. Geosci.* **9**, 843–847 (2016).
41. Westerhold, T. et al. An astronomically dated record of Earth’s climate and its predictability over the last 66 million years. *Science* **369**, 1383–1387 (2020).
42. Gersonde, R. & Censarek, B. Middle–late Southern Ocean climate development and its implication on Antarctic ice sheet development—diatom evidence from Atlantic sector ODP Sites. *Geophys. Res. Abstr.* **8**, 06285 (2006).
43. Groeneveld, J. et al. Australian shelf sediments reveal shifts in Miocene Southern Hemisphere westerlies. *Sci. Adv.* **3**, e1602567 (2017).
44. Sun, T., Xu, Z., Chang, F. & Li, T. Climate evolution of southwest Australia in the Miocene and its main controlling factors. *Sci. China Earth Sci.* **65**, 1104–1115 (2022).
45. Xing, Q. et al. The sensitivity of the Eocene–Oligocene Southern Ocean to the strength and position of wind stress. *Clim. Past* **18**, 2669–2693 (2022).
46. Escutia, C. et al. Cenozoic ice sheet history from East Antarctic Wilkes Land continental margin sediments. *Glob. Planet. Change* **45**, 51–81 (2005).
47. Huang et al. Depositional and erosional signatures in sedimentary successions on the continental slope and rise off Prydz Bay, East Antarctica—implications for Pliocene paleoclimate. *Mar. Geol.* **430**, 106339 (2020).

48. Sokolov, S. & Rintoul, S. R. On the relationship between fronts of the Antarctic Circumpolar Current and surface chlorophyll concentrations in the Southern Ocean. *J. Geophys. Res.* **112**, C07030 (2007).
49. Schlitzer, R. Ocean Data View (v.5.6.7); <https://odv.awi.de> (2023).
50. Hoem, F. S. et al. Strength and variability of the Oligocene Southern Ocean surface temperature gradient. *Commun. Earth Environ.* **3**, 322 (2022).

Publisher's note Springer Nature remains neutral with regard to jurisdictional claims in published maps and institutional affiliations.

Open Access This article is licensed under a Creative Commons Attribution 4.0 International License, which permits use, sharing,

adaptation, distribution and reproduction in any medium or format, as long as you give appropriate credit to the original author(s) and the source, provide a link to the Creative Commons license, and indicate if changes were made. The images or other third party material in this article are included in the article's Creative Commons license, unless indicated otherwise in a credit line to the material. If material is not included in the article's Creative Commons license and your intended use is not permitted by statutory regulation or exceeds the permitted use, you will need to obtain permission directly from the copyright holder. To view a copy of this license, visit <http://creativecommons.org/licenses/by/4.0/>.

© The Author(s) 2024

Methods

Age model

The age model for DSDP Site 278 cores 31R to 26R is from ref. 10. An age–depth model for the DSDP Site 278 cores 25R to 2R (~329–100 m below seafloor) was developed from the revision and integration of calcareous nannofossil, marine diatom and radiolarian biostratigraphy, calibrated using *The Geologic Time Scale 2012*⁵¹. Our updated age interpretation for the sediments between cores 25R and 2R spans an interval from ~21.3 to 0.5 Ma (Extended Data Fig. 1). Detailed discussion on the development of the age model is presented in ref. 10. The age model for the lower Miocene and Pleistocene intervals of ODP Site 744 Hole B was developed from the revision of marine diatom, radiolarian biostratigraphy and magnetostratigraphic data calibrated using *The Geologic Time Scale 2012*⁵¹ (Extended Data Fig. 2). Diatom and radiolarian biostratigraphic data were compiled from a variety of published sources^{52,53}. The magnetic stratigraphy of ODP Site 744 was compiled from refs. 19,54.

Fossil fish debris sample preparation for neodymium isotope analyses

Fish teeth and bones (fish debris) were handpicked from the >63 µm sediment fractions isolated by wet sieving. A total of 31 samples from Site 278 and 91 samples from Site 744 were selected for fish debris Nd isotope analyses. All samples were treated with ultraclean 18 MΩ water and methanol following ref. 55 to remove debris from surfaces and cavities (see also ref. 56). Cleaned fish debris samples were subsequently transferred into pre-cleaned microcentrifuge tubes and dissolved overnight in 50 µl of 2 M HCl. Dissolved fish debris samples were loaded on Biorad cation exchange resin (200–400 µm mesh) to separate the rare earth elements (REEs) from the sample matrix and Eichrom Ln-Spec resin (50–100 µm bead size) to separate Nd from the other REEs. In addition, 49 dissolved fish debris samples from ODP Site 744 (early to late Miocene) were cleaned with the same methodology. Cleaned fish debris samples were subsequently transferred into pre-cleaned microcentrifuge tubes and dissolved overnight in 50 µl of 3 M HNO₃. Dissolved fish debris samples were loaded on Tru-spec resin to separate the REEs from the sample matrix and Ln-Spec resin chromatography to separate Nd from the other REEs.

Bulk sediment sample preparation for neodymium isotope analyses

Two samples from Site 278 were selected to determine the detrital sediment Nd isotope composition to evaluate the potential contribution of the detrital sediments to the porewaters and/or overlying bottom-water signatures. Samples were dried and gently homogenized using mortar and pestle. First, 1.5 g dried sample and 70–75 ml 1.5% buffered acetic acid solution were used to remove biogenic carbonate (carbonate leaching). Exchangeable ions were subsequently removed using 10 ml 1 M MgCl₂ solution. In a third step, ferromanganese oxides and oxyhydroxides were removed using leaching in a weak reductive solution of 0.005 M hydroxylamine hydrochloride (NH₂OH), 1.5% acetic acid and 0.03 M Na₂-EDTA for 1 h, followed by a stronger leaching step utilizing 0.05 M NH₂OH for 17 h. Subsequently, 50 mg of leached and water washed detrital sediment was digested on a hotplate using a mixture of 1 ml concentrated HNO₃, 0.8 ml HClO₄ and 2 ml HF. The detrital samples were processed using the same column chromatography as the fish debris from Site 278.

Neodymium isotope measurements

Neodymium isotope ratios for fish debris and detrital sediment samples from Site 278 were determined on a Nu Plasma multicollector inductively coupled plasma mass spectrometer (MC-ICP-MS) at Imperial College London, operated in static mode. Instrumental mass bias was corrected using the ¹⁴⁶Nd/¹⁴⁴Nd ratio of 0.7219. A JNdi-1 isotope standard was run after every sample, and all reported ¹⁴³Nd/¹⁴⁴Nd

ratios were corrected to a JNd_i ¹⁴³Nd/¹⁴⁴Nd ratio of 0.512115 (ref. 57) using bracketing standards. External reproducibility was monitored using JNd_i standards, and accuracy was confirmed by measuring USGS BCR-2 rock standards with each batch of samples, yielding average ¹⁴³Nd/¹⁴⁴Nd ratios of 0.512636 ± 0.000010 ($n = 17$; 2 s.d.) in excellent agreement with the published BCR-2 ¹⁴³Nd/¹⁴⁴Nd ratio of 0.512638 ± 0.000015 (ref. 58).

Neodymium isotope ratios for 42 fish debris samples from Site 744 were determined using a Thermo Scientific Triton Plus thermal ionization mass spectrometer at the Observatoire Midi-Pyrenees. Samples were dissolved in 200 µl of 0.05 M HNO₃ and loaded on degassed rhenium filaments. Measured ¹⁴³Nd/¹⁴⁴Nd ratios are an average of 150 measurements of ion intensities following the static multi-collection mode. Instrumental mass bias was corrected using the ¹⁴⁶Nd/¹⁴⁴Nd ratio of 0.7219. During the whole measurement period, 13 Rennes standards were measured repetitively to determine the internal reproducibility. The Rennes measurements gave a mean ¹⁴³Nd/¹⁴⁴Nd isotope ratio of 0.511953 ± 0.00004 (2 s.d., $n = 13$), in agreement with published Rennes ¹⁴³Nd/¹⁴⁴Nd ratio of 0.511961 ± 0.000013 ref. 59).

Neodymium isotope ratios for 49 fish debris samples from Site 744 were performed using a Plasma 3 MC-ICP-MS (Nu Instruments–AME-TEK) at Centres Científics i Tecnològics of the Universitat de Barcelona. The ¹⁴³Nd/¹⁴⁴Nd instrumental mass bias was corrected using the reference ¹⁴⁶Nd/¹⁴⁴Nd ratio of 0.7219. Moreover, a JNdi-1 standard was analysed before and after each sample, and an additional sample-standard bracketing normalization of the mass bias-corrected ratios was carried out using the reference ¹⁴³Nd/¹⁴⁴Nd value of 0.512115 ± 0.000007 for this standard⁵⁷. Uncertainties of the ϵ_{Nd} values correspond to the external reproducibility of the JNdi-1 analysis performed throughout each measurement session (2 s.d., $n = 22$ –34). Uncertainties were 0.14 to 0.21 ϵ_{Nd} units. The accuracy of the method has been demonstrated through multiple analyses of the AMES II standard (0.511973 + / – 0.000012, 2 s.d. = 24 ppm, $n = 116$), and results were not significantly different from those previously published²⁴. Procedural blanks were systematically negligible with the three methods.

REE concentrations

The REE concentration measurements from 39 fish debris samples at Site 744 were made on aliquots of the same samples used for Nd isotope analysis, using a Thermo Scientific Element XR high-resolution ICP-MS at the Observatoire Midi-Pyrenees. Indium and Rhenium were used as internal standards during ICP-MS measurements to monitor instrumental drift during the course of the analyses. The instrument was calibrated using a synthetic multi-element solution routinely used by the Observatoire Midi-Pyrenees ICP-MS service. This calibration solution has been analysed with three different dilution factors, at the beginning and at the end of the analyses, to calibrate the instrument response and correct the drift along the analytical sequence. Oxide interferences (BaO⁺ on Nd⁺ and Eu⁺, light REE on intermediate REE and intermediate REE on heavy REE) were then corrected. However, these interferences were very low since the samples were injected via an ARIDUS II desolvating nebulizer system. The precision and accuracy of ICP-MS analyses were assessed by measuring the natural river water reference materials SLRS 6. All REE data were normalized to post-Archaeon shale concentrations⁶⁰.

To correct for the in situ decay of ¹⁴⁷Sm to ¹⁴⁴Nd within the fish debris at Site 278 over time, we used a site-specific average ¹⁴⁷Sm/¹⁴⁴Nd ratio of 0.1365, based on samples of fish debris measured from older parts at the same site¹⁰. For Site 744, we used the ¹⁴⁷Sm/¹⁴⁴Nd ratio for sample that we measured Sm and Nd concentrations and a site-specific average ¹⁴⁷Sm/¹⁴⁴Nd ratio of 0.1333 based on samples of fish debris measured from older parts at the same site²⁰. Corrections for the in situ decay of ¹⁴⁷Sm to ¹⁴⁴Nd amounted to 0.01–0.16 ϵ_{Nd} units for both sites. Decay-corrected ratios are denoted with (t) in all figures and text.

Grain-size analyses

Grain-size analyses were performed at the Environnements et Paléoenvironnements Océaniques et Continentaux (University of Bordeaux). Bulk grain size was measured in a total of 44 samples from Site 278: 28 samples from cores 2R–25R and 16 samples from cores 26R–34R using a laser microgranulometer Malvern mastersizer hydro 2000G with automatic samples (0.020 to 2,000 μm). To separate the terrigenous sediment fraction, we used 1–2 ml HCl 37% (hydrochloric acid) to dissolve carbonate and 20 ml H_2O_2 (hydrogen peroxide) to remove organic carbon. Moreover, to remove the biogenic (opaline) silica, samples were separated into two groups: (1) sediments with low silica content and (2) sediments with high silica content. For the first group, 40 ml Na_2CO_3 (2 M) (sodium carbonate) was used, while 20 ml NaOH (1 M) (sodium hydroxide) was used for sediments with high silica content. Smear slides were prepared to verify efficient removal of siliceous microfossils under a microscope at $\times 500$ magnification.

To reconstruct the current speed, we focused on the 10–63 μm terrigenous sediment fraction—the sortable silt range (SS)²². Particles smaller than 10 μm are deposited as aggregates due to cohesion and thus cannot be used as a proxy for current velocity, whereas the sediment fraction between 10 and 63 μm has been documented to reflect current sorting in most cases²². The mean sortable silt size of the 10–63 μm terrigenous sediment fraction (\overline{SS}) was calculated in all 44 samples at Site 278 after the removal of carbonates, organic matter and biogenic silica. Precision of the method was $\pm 3\%$.

Model simulations

To understand the role of the tectonic opening of the 53.5° S passage within the Macquarie Ridge complex on local ocean circulation and ACC strengthening, we ran two model simulations, with the only change being the ridge bathymetry, using the primitive equation Massachusetts Institute of Technology general circulation model⁶¹. The model simulations were limited to a regional domain, extending from 145 to 175° E and 48 to 60° S. We used open boundary conditions with steady-state, annual mean temperature, salinity and velocity fields from the Southern Ocean State Estimate⁶². The circulation was restored to these boundary conditions along a 1° wide sponge along all lateral boundaries. Sea surface temperatures and salinities were restored to steady annual mean fields with a restoring timescale of ten days. The wind stress was also a steady mean field from Southern Ocean State Estimate. The model configurations used a free surface, free-slip boundary conditions, a quadratic bottom drag with a coefficient of 0.002 and a nonlinear equation of state⁶³.

The model configurations used a horizontal resolution of $1/20^\circ$ and 200 vertical levels ranging from 4 m at the surface to 40 m at depth. The maximum ocean depth is 6,000 m. The modern-day bathymetry was taken from the Shuttle Radar Topography Mission, SRTM30_PLUS^{64,65}. The model configuration with the ‘open’ passage was the same as used by ref. 66. To test how much the 53.5° S passage hampers the ACC flow across the ridge, we ran a second model where the bathymetry was modified, adjusting the depth of the 53.5° S passage to ~ 500 m to be aligned with the surrounding ridge depth (‘closed ridge’ configuration). The model was run for 20 years, with the figures showing output averaged over the last 10 years.

Data availability

The datasets generated as part of this study are available at PANGAEA (<https://doi.pangaea.de/10.1594/PANGAEA.937372>).

References

- Gradstein, F. M., Ogg, J. G., Schmitz, M. D. & Ogg, G. M. *The Geologic Time Scale 2012* (Elsevier, 2012).
- Baldauf, J. G. & Barron, J. A. Diatom biostratigraphy: Kerguelen Plateau and Prydz Bay regions of the Southern Ocean. In *Proc. Ocean Drilling Program Scientific Results* Vol. 119 (eds Barron, J. et al.) 547–598 (ODP, 1991).
- Barron, J. et al. *Proc. Ocean Drilling Program Initial Reports* Vol. 119 (ODP, 1991).
- Florindo, F. et al. Paleomagnetism and biostratigraphy of sediments from Southern Ocean ODP Site 744 (southern Kerguelen Plateau): implications for early to middle Miocene climate in Antarctica. *Glob. Planet. Change* **110**, 434–454 (2013).
- Martin, E. E. & Haley, B. A. Fossil fish teeth as proxies for seawater Sr and Nd isotopes. *Geochim. Cosmochim. Acta* **64**, 835–847 (2000).
- Huck, C. E., van de Flierdt, T., Bohaty, S. M. & Hammond, S. J. Antarctic climate, Southern Ocean circulation patterns, and deep water formation during the Eocene. *Paleoceanography* **32**, 674–691 (2017).
- Tanaka, T. T. et al. JNdi-1: a neodymium isotopic reference in consistency with LaJolla neodymium. *Chem. Geol.* **168**, 279–281 (2000).
- Weis, D. et al. High-precision isotopic characterization of USGS reference materials by TIMS and MC-ICP-MS. *Geochem. Geophys.* **7**, Q08006 (2006).
- Chauvel, C. & Blichert-Toft, J. A hafnium isotope and trace element perspective on melting of the depleted mantle. *Earth Planet. Sci. Lett.* **190**, 137–151 (2001).
- Taylor, S. R. & McLennan, S. M. *The Continental Crust: Its Composition and Evolution* (Blackwell, 1985).
- Marshall, J., Adcroft, A., Hill, C., Perelman, L. & Heisey, C. A finite-volume, incompressible Navier Stokes model for studies of the ocean on parallel computers. *J. Geophys. Res. Oceans* **102**, 5753–5766 (1997).
- Mazloff, M. R., Heimbach, P. & Wunsch, C. An eddy-permitting Southern Ocean state estimate. *J. Phys. Oceanogr.* **40**, 880–899 (2010).
- Jackett, D. R. & McDougall, T. J. Minimal adjustment of hydrographic profiles to achieve static stability. *J. Atmos. Ocean Technol.* **12**, 381–389 (1995).
- Becker, J. J. et al. Global bathymetry and elevation data at 30 arc seconds resolution: SRTM30_PLUS. *Mar. Geod.* **32**, 355–371 (2009).
- Sandwell, D. T. & Smith, W. H. F. Global marine gravity from retracked Geosat and ERS-1 altimetry: ridge segmentation versus spreading rate. *J. Geophys. Res. Solid Earth* **114**, B01411 (2009).
- Zhang, X. & Nikurashin, M. Small-scale topographic form stress and local dynamics of the Southern Ocean. *J. Geophys. Res. Oceans* **125**, e2019JC015420 (2020).
- Scher, H. D. & Martin, E. E. Circulation in the Southern Ocean during the Paleogene inferred from neodymium isotopes. *Earth Planet. Sci. Lett.* **228**, 391–405 (2004).
- Frank, M., Whiteley, N., Kasten, S., Hein, J. R. & O’Nions, K. North Atlantic Deep Water export to the Southern Ocean over the past 14 Myr: evidence from Nd and Pb isotopes in ferromanganese crusts. *Paleoceanography* **17**, 1022 (2002).
- Dausmann, V., Frank, M., Gutjahr, M. & Rickli, J. Glacial reduction of AMOC strength and long-term transition in weathering inputs into the Southern Ocean since the mid-Miocene: evidence from radiogenic Nd and Hf isotopes. *Paleoceanogr. Paleoclimatol.* **32**, 265–283 (2017).
- Burton, K. W., Ling, H.-F. & O’Nions, R. K. Closure of the Central American Isthmus and its effect on deep-water formation in the North Atlantic. *Nature* **386**, 382–386 (1997).
- Ling, H. F. et al. Evolution of Nd and Pb isotopes in Central Pacific seawater from ferromanganese crusts. *Earth Planet. Sci. Lett.* **146**, 1–12 (1997).
- van de Flierdt, T. et al. Deep and bottom water export from the Southern Ocean to the Pacific over the past 38 million years. *Paleoceanography* **19**, PA1020 (2004).

73. Le Houedec, S., Meynadier, L. & Allégre, C. J. Seawater Nd isotope variation in the Western Pacific Ocean since 80 Ma (ODP 807, Ontong Java Plateau). *Mar. Geol.* **380**, 138–147 (2016).

Acknowledgements

This research used samples provided by the International Ocean Discovery Program (IODP). We acknowledge the staff and shipboard party from Leg 28 and Leg 119. We thank the staff at the Gulf Coast core repository (GCR) for curating these cores and for assistance in core handling and shipping. Funding for this research is provided by the Spanish Ministry of Economy, Industry and Competitiveness (grant CTM2017-89711-C2-1/2-P; PID2021-126495NB-C31), co-funded by the European Union through FEDER funds. D.E. was funded by the Alexander S. Onassis Public Benefit Foundation PhD research grant (F ZL 016-1/2015-2016), by MOPGA postdoctoral visiting fellowship programme funded by the French Ministry of Europe and Foreign Affairs (grant MOPGA postdoc-3–5669831615), by the Juan de la Cierva-formation postdoctoral research grant (FJC2020-043650-I) funded by MCIN/AEI/ 10.13039/501100011033 and the ‘European Union NextGenerationEU/PRTR’ and by the UK Research and Innovation Engineering and Physical Sciences Research Council (grant number EP/X02623X/1). D.E. received additional funding from an ECORD research grant and IODP-France. I.S. and A.K. were supported by the Australian Research Council Special Research Initiative for Antarctic Gateway Partnership (project ID SR140300001) and the Australian Research Council’s Discovery Project 180102280. Model runs were undertaken with the assistance of resources from the National Computational Infrastructure (NCI), which is supported by the Australian Government. We thank the Paleomagnetic Laboratory CCiTUB-Geo3Bcn CSIC for the support on palaeomagnetic analysis. The GRC Geociències Marines thanks the Generalitat de Catalunya for the Grups de Recerca Consolidats grant 2021SGR01195 and for the ICREA-Academia award to I.C. This paper is a contribution to the SCAR INSTANT Programme.

Author contributions

D.E. and C.E. designed and led the research aided by J.E. and X.C. D.E. conducted the Nd isotope analyses with assistance from K.K. and T.v.d.F. at Imperial College, M. Benoit, M. Belhadj and C.J. at Observatoire Midi Pyrénées and E.P., E.G.-S., L.D.P. and I.C. at University of Barcelona. D.E. and M. Belhadj produced the REE data. D.E. produced the grain-size data with input from E.D. I.S. and A.K. carried out the general circulation model. J.-A.F., L.V. and D.M.H. improved the age model. A.L.-Q. and A.S. provided input with deep-sea sedimentary processes. D.E. created the figures and wrote the paper with assistance from all authors.

Competing interests

The authors declare no competing interests.

Additional information

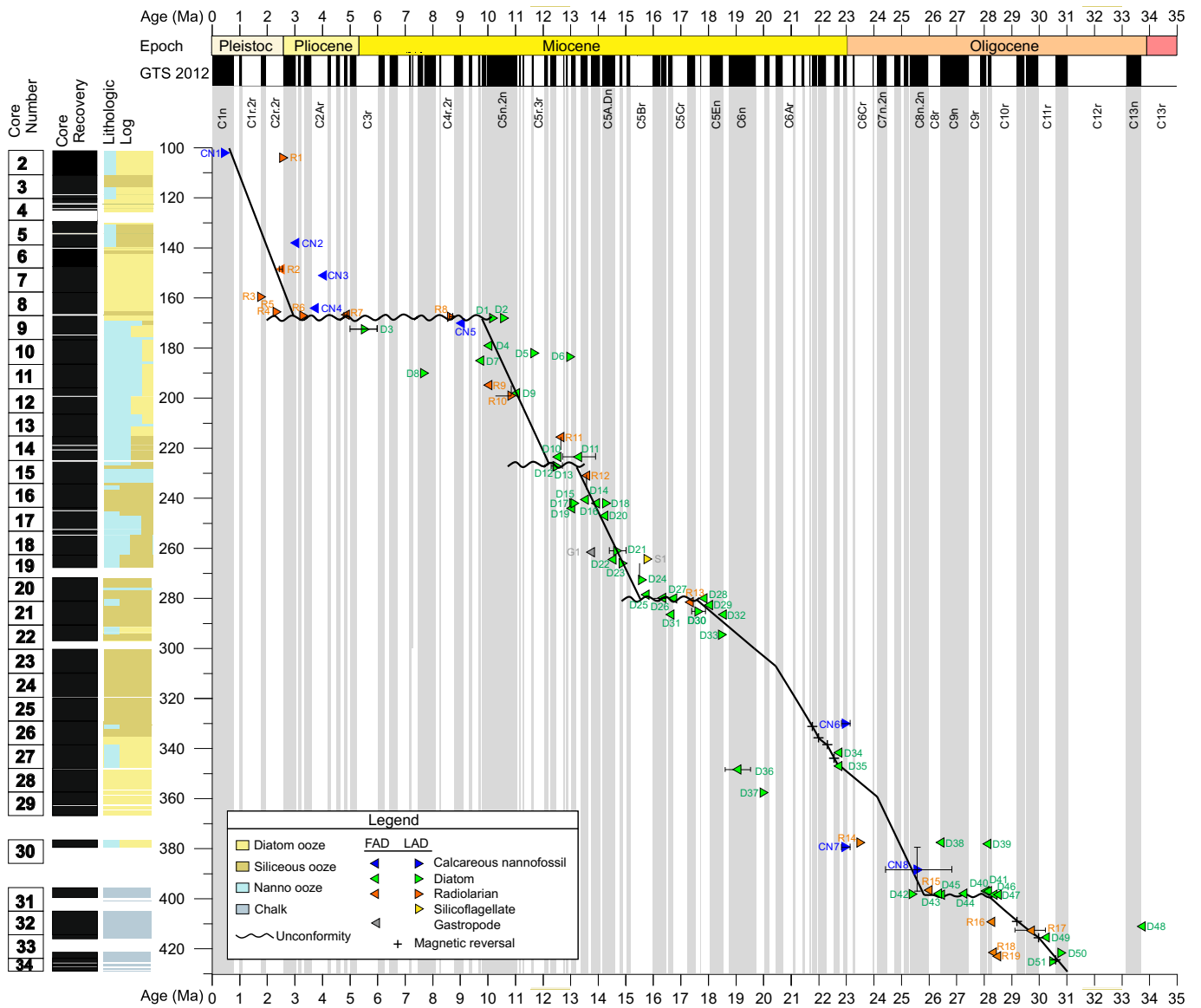
Extended data is available for this paper at <https://doi.org/10.1038/s41561-023-01356-3>.

Supplementary information The online version contains supplementary material available at <https://doi.org/10.1038/s41561-023-01356-3>.

Correspondence and requests for materials should be addressed to Dimitris Evangelinos.

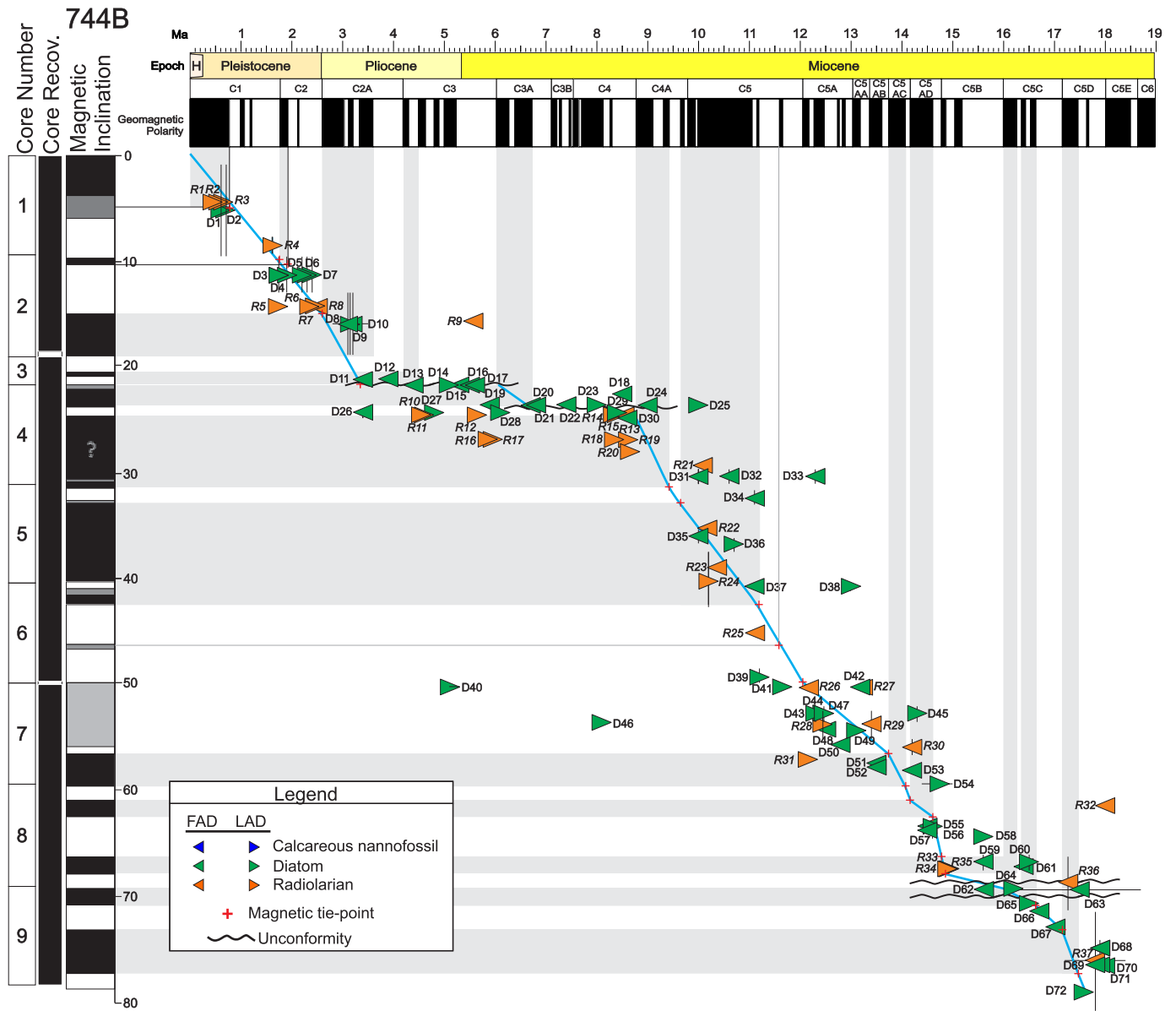
Peer review information *Nature Geoscience* thanks Bella Duncan and the other, anonymous, reviewer(s) for their contribution to the peer review of this work. Primary Handling Editors: James Super and Thomas Richardson in collaboration with the *Nature Geoscience* team.

Reprints and permissions information is available at www.nature.com/reprints.



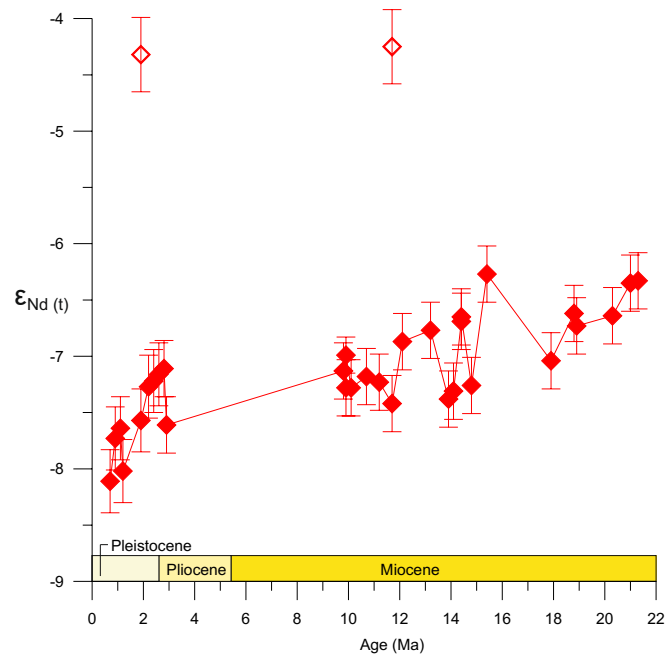
Extended Data Fig. 1 | Revised age-depth model at Site 278. From left to right: core number, core recovery, lithologic log based on initial shipboard sedimentological descriptions, depth in meters below sea floor (mbsf). Grey vertical stripes show normal polarity zones of the geomagnetic polarity

timescale⁵¹. LAD: Last appearance datum, FAD: First appearance datum. Horizontal error bars on biostratigraphic events indicate total age range for the given datum. Vertical error bars indicate the depth range for the given datum. Datums for cores 34R-26R are from¹⁰.

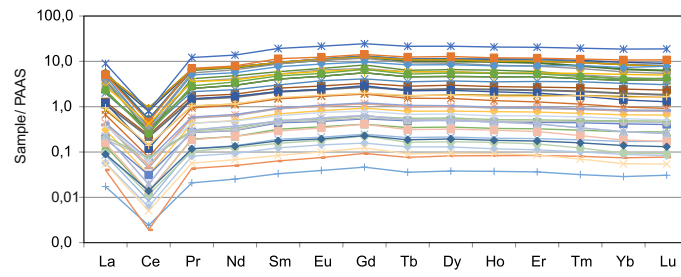


Extended Data Fig. 2 | Revised age-depth model at Site 744 Hole B. From left to right: core number, core recovery, local polarity based on inclination values^{19,54} and depth in meters below sea floor (mbsf). Grey vertical stripes show normal polarity zones of the geomagnetic polarity timescale⁵¹. LAD: Last appearance

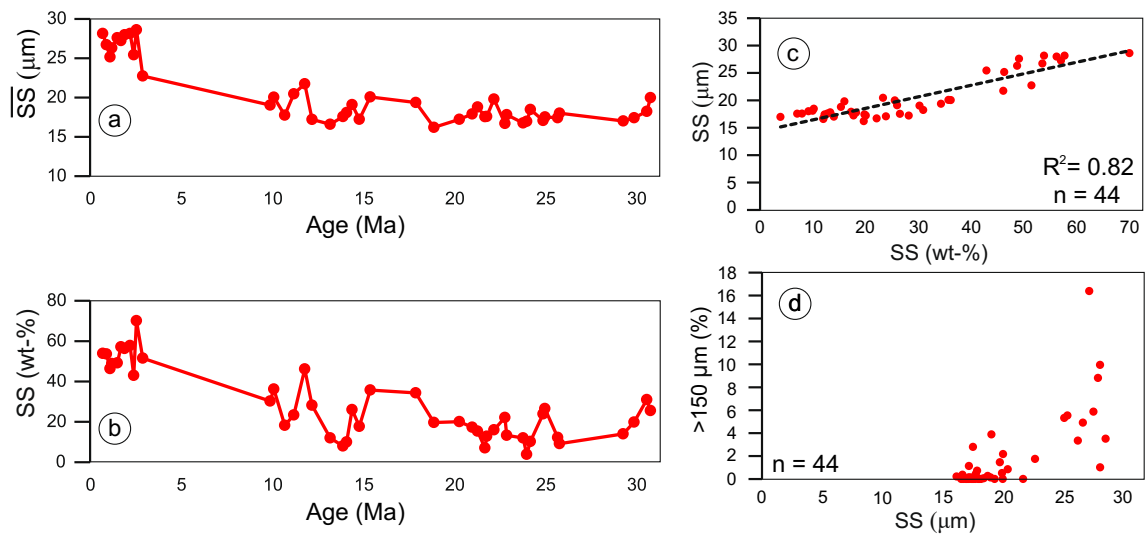
datum, FAD: First appearance datum. Horizontal error bars on biostratigraphic events indicate total age range for the given datum. Vertical error bars indicate the depth range for the given datum.



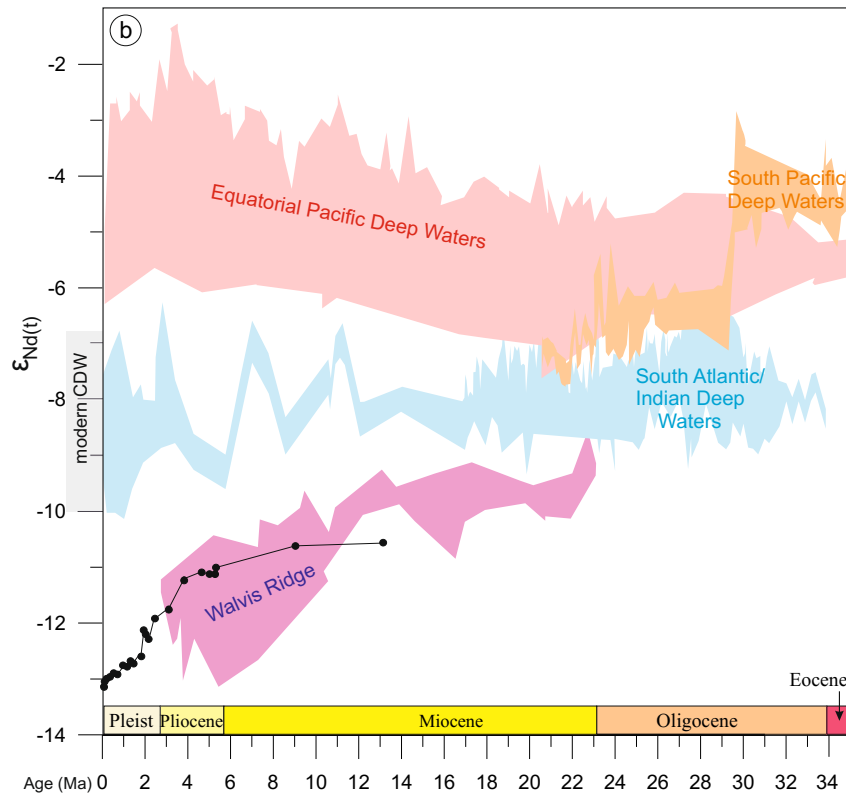
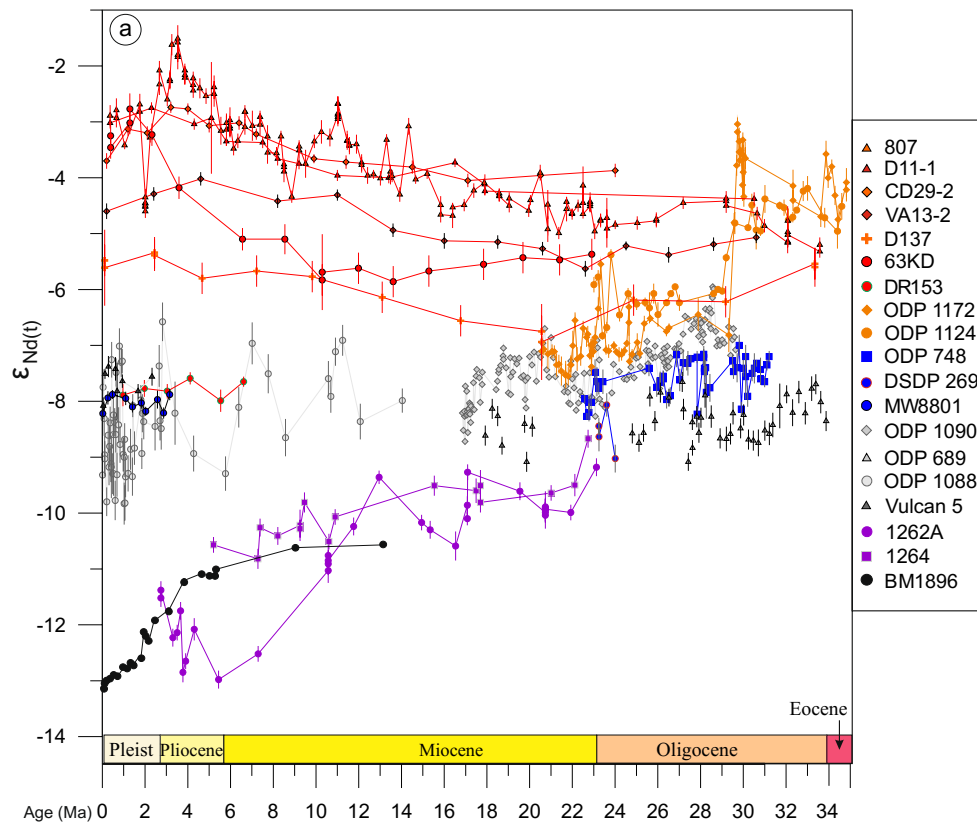
Extended Data Fig. 3 | Neodymium isotope data from Site 278. Neodymium isotope composition ($\epsilon_{Nd(t)}$) of fish debris (red filled diamonds; $n = 31$) and bulk sediment $\epsilon_{Nd(t)}$ values (red open diamonds) at Site 278. Error bars represent instrumental uncertainty (2σ).



Extended Data Fig. 4 | Rare earth element patterns normalized to Post Archean Shale (PAAS) concentrations from fish debris data at Site 744.



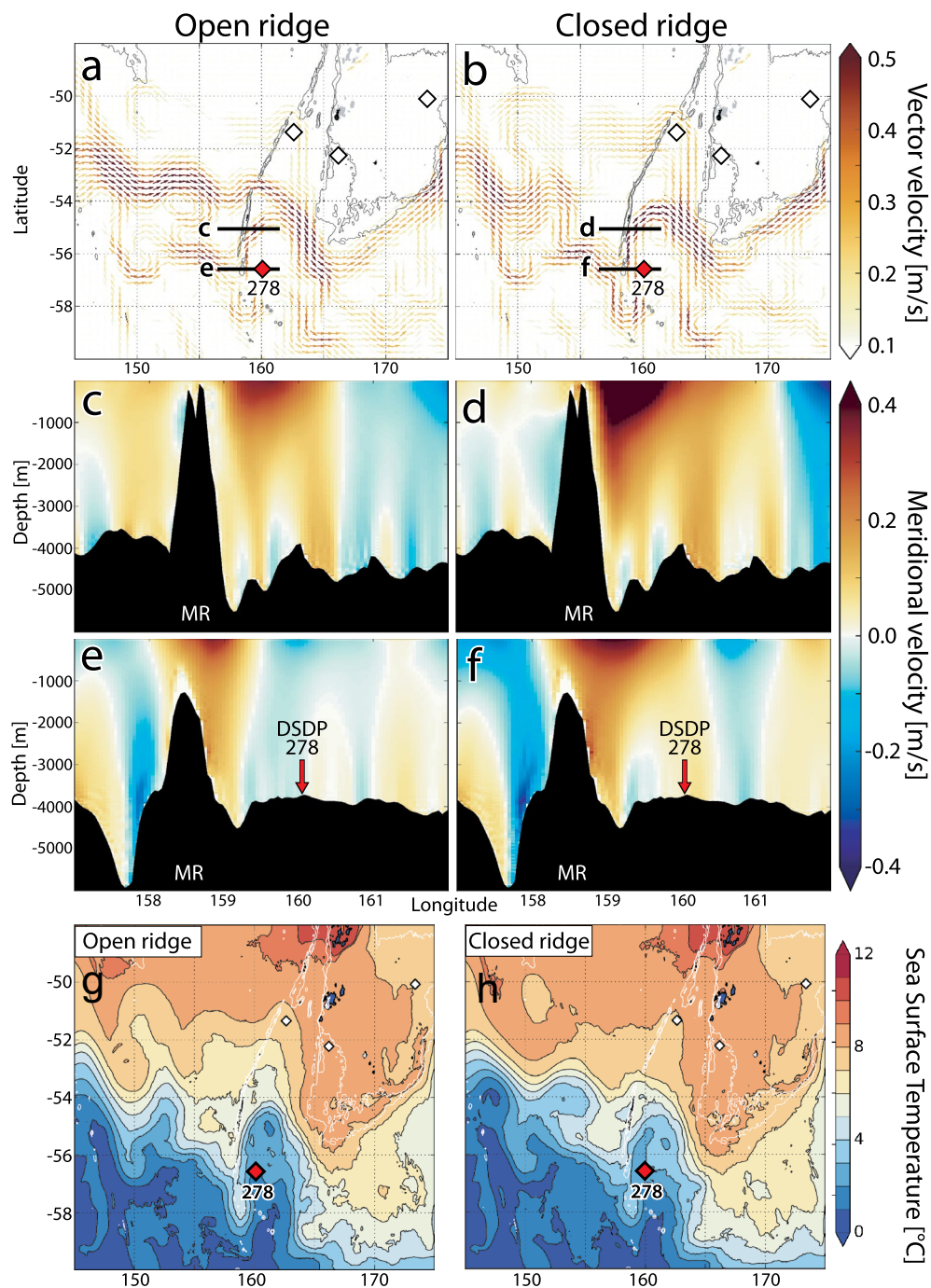
Extended Data Fig. 5 | Down-core grain size data from Site 278. a: Mean sortable silt (\overline{SS}), **b:** Site 278 sortable silt (SS) percentage, **c:** Linear relation between \overline{SS} and SS percentage, **d:** uncorrelated IRD ($> 150 \mu\text{m}$) with SS.



Extended Data Fig. 6 | See next page for caption.

Extended Data Fig. 6 | Water-mass endmembers and Nd isotope records used for this study from the Atlantic, Indian and Pacific Oceans. For site locations see Fig. 1. **a**, Individual Nd isotope records. **b**, Water-mass endmembers for the Atlantic, Indian and Pacific Oceans. The South Atlantic/Indian Ocean deep water endmember is based on sites ODP Site 689 (Maud Rise; $n = 45$)⁶⁷, Vulcan 5 ($n = 4$)⁶⁸, ODP 1088 ($n = 60$)⁶⁹ and ODP 1090 ($n = 181$)²⁴ (Agulhas Ridge) ODP Sites 748 (Kerguelen Plateau; $n = 49$)²⁰, MW8801 ($n = 10$)⁶⁸ and DSDP Site 269 (off Adélie Coast; $n = 4$)³⁶. The Walvis Ridge endmember is based on ODP Sites 1262 ($n = 31$) and 1264 ($n = 16$) (Walvis Ridge²³). Crust BM1969 (San Pablo seamount;

black dots; $n = 23$)⁷⁰ is located in the northwest Atlantic Ocean. The South Pacific deep water endmember is based on ODP Site 1124 (Hikurangi Plateau; $n = 36$)⁸ and ODP Site 1172 (East Tasmanian Plateau; $n = 75$)⁸. Other indications for the composition of deep waters in the South Pacific/Tasman Sea come from crust DR153 (Southeast Pacific; $n = 6$)⁶⁸. The Equatorial Pacific endmember is based on crusts from Central Pacific: D11-1 ($n = 14$)⁷¹, VA13-2 ($n = 14$)⁷¹, CD29-2⁷¹ ($n = 14$) and crust 63KD (Tasman Sea; $n = 17$)⁷², D137 (Nova Canton Trough; $n = 15$)⁷⁰ and carbonate fraction from ODP 806 (Ontong Java Plateau; $n = 138$)⁷³. Error bars represent instrumental uncertainties (2σ).



Extended Data Fig. 7 | Oceanographic model results with an open (present-day) and closed (Pliocene) 53.5°S Macquarie Ridge passage (left and right, respectively). Upper panels (a, b): vector plots of surface ocean current velocities at 100 m water depth (annual mean). Locations of key drill site (DSDP 278, red diamond), other drill sites (white diamonds), depth profiles (c-f) and depth contours (0 m, 1000 m, 2000 m; black lines) are shown. Middle panels (c-f): depth profiles of annual mean meridional velocities across the ridge

(red, blue - north-/southward, respectively; black regions - below seafloor; red arrow - location of DSDP 278 site). Bottom panels (g, h): annual mean sea surface temperatures (at 100 m water depth) with an open (present-day) and closed (Pliocene) 53.5°S Macquarie Ridge passage (left and right, respectively). The model was run for 20 years, with the figures showing output averaged over the last 10 years.